Challenges in Sub-Surface Fluorescence Diffuse Optical Imaging

Dax Kepshire[1], Scott Davis[1],
Hamid Dehghani[1,2], Keith D. Paulsen[1], Brian W. Pogue[1]
Thayer School of Engineering, Dartmouth College, Hanover NH
Department of Physics, University of Exeter, UK

ABSTRACT

A fully non-contact CCD-based approach to sub-surface fluorescence diffuse optical imaging is presented. An overview of CCD-noise sources are described and a possible solution for obtaining an adequate SNR in CCD-based diffuse optical imaging is implemented. To examine the impact of excitation and remission light attenuation in this geometry, the linearity of response in recovering object position was examined in simulations, with respect to changes in target size, target-to-background contrast, and depth. To provide insight regarding the technological complications of sub-surface imaging, liquid phantom experiments were performed for targets of size 4mm, 8mm and 14mm having 10:1 target-to-background contrast. Overall, the results indicate that steps must be taken to eliminate blooming artifacts, perhaps by physically blocking the active source as it is projected onto the CCD chip. In general, response linearity in the recovered target centroid position, size, and fluorophore concentration as well as complications arising due to partial volume sampling effects are expected to improve if prior structural images obtained from another modality are incorporated into the DOT reconstruction algorithm.

INTRODUCTION

The potential for diffuse optical tomography to serve as a noninvasive modality for functional and metabolic imaging of tissue has been comprehensively analyzed for clinical use [1-3]. The majority of these systems, however, utilize a transmission-based approach for measuring the absorption and scattering of light in tissue, as illustrated in Figure 1 (a). Subsequently, attenuation and diffusion constraints limit this type of DOT to a few specific anatomical sites, most commonly the female breast. Sub-surface-mode tomography (Figure 1 (b)) however has the potential to serve as a full human body diagnostic imaging modality, because it allows light to be delivered and collected from the same side of the tissue surface. Sub-surface imaging is not without its problems however. An earlier study recently demonstrated that the recovery of target fluorophore concentration and size is non-linear with depth in this geometry, but that the target centroid position of the target can be recovered [4] when optical techniques alone are used.

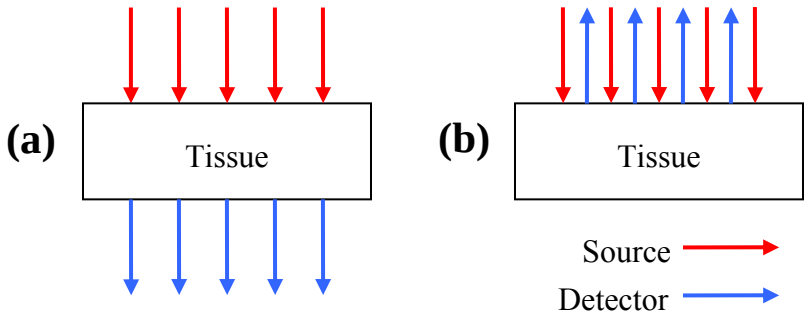

Figure 1: An illustration presenting the two most common geometries that have been previously investigated for fluorescence diffuse optical tomography. The primary difference is that transmission-based tomography systems (a) collect light as it is transmitted through the tissue whereas sub-surface systems (b) deliver and collect light from the same side of the tissue.

Though sub-surface tomography has been investigated for some time in studying brain activation [5-8], and as a diagnostic tool for breast cancer screening[9], there are many physical and technological challenges inherent to sub-surface tomography which must be addressed before full body diffuse optical imaging of human subjects becomes a reality. This not only includes understanding the attenuation constraints inherent to this geometry and possibly the insurmountable issues this poses, but also the technological challenges arising due to the non-contact CCD-based measurements of the photon diffusion in tissue.

2. MATERIALS AND METHODS

2.1 Instrumentation

The non-contact fluorescence diffuse optical tomography (FDOT) imaging system utilized in this study has previously been presented in great detail [4]. Optimized for imaging Protoporphyrin IX (Pp-IX), this FDOT system utilizes a pair of orthogonal galvanometers to allow the 635 nm collimated diode laser source to raster scan across the tissue/phantom surface. The diffuse reflectance and remission intensity signals are separated by a 632 nm narrow band interference filter and a 650 long pass optical filter respectively before being projected onto the surface of a cooled 12-bit CCD camera. For each source position 15 measurements of the diffuse fluorescence intensity were acquired to form a full dataset of 240 measurements in approximately 1.5 minutes. As this is a non-contact based system, the signal for each of the 15 'virtual detectors' was obtained by averaging individual groups of 16 X 16 pixels in an area of 2.5×2.5 mm^2. The total field of view (FOV) under examination was comprised of an area of 4×0.25 cm^2.

2.2 Optimizing Non-contact-based Detection

In reconstructing DOT images it is pertinent that the experimental data matches the mathematical model. Data with a poor signal-to-noise or data that is not calibrated properly will inevitably result in a failed reconstruction or an image dominated by artifacts. Because this system is fully non-contact, the greatest source of data error is not due to coupling of the sources and detectors at the phantom or tissue interface, but rather problems inherent to the CCD device itself – most prominently CCD noise, blooming, and a poor SNR at detectors located far from the source.

The primary sources of noise in a CCD camera include shot noise (n_{shot}), readout noise (n_{read}), and dark noise (n_{dark}). Shot noise is due to the statistical variation in the rate at which photons arrive at and interact with the CCD's semiconductive material. In general, CCD shot noise follows a Poisson distribution and can be equivalently expressed as:

$$n_{shot} \equiv N^{1/2} \tag{1}$$

where N is the number of counts measured in a single pixel. For most applications, shot noise is the dominant source of noise because it is a function of the intensity of the incident light. The exception however would be low light applications; in this scenario readout noise, or noise produced during the analog-to-digital conversion is dominant. In this system, or other CCD based DOT systems for that mater, this phenomenon can be observed at the detectors located far from the source (> 2cm). One possible solution for avoiding these read-noise limited situations, and thereby maintaining an appropriate SNR at all detector locations, is discussed below. The final source of noise, the dark noise, is due to statistical variation in the thermally generated electrons within the semiconductor substrate; because the dark noise is a random variation in the dark signal it cannot be removed. In the raw datasets however the dark signal must be removed prior to calibration. Because the magnitude of the dark signal depends on the CCD temperature and increases linearly with increasing integration time, it can be accounted for by recording the dark signal as function of increasing integration time and by then using the equation obtained from a linear polynomial fit to remove the dark signal from the raw data as it is acquired.

A major problem with non-contact CCD-based imaging lies in the fact that when individual pixels in the CCD reach saturation (due to a very strong signal) the electrons occupying individual pixel wells can actually overflow into the neighboring wells in a phenomenon known as blooming. An example of CCD blooming as observed using this system is demonstrated in Figure 2. In the first image (a) an integration time of 50ms is used and it appears that the full well capacity (red pixels) of a small group of pixels within that virtual detector has been reached. Here, blooming does not occur as this is the actual spot size of the laser diode source. In the second image (b), an integration time of 500ms is used and the blooming phenomenon becomes apparent. It now appears that the laser spot actually occupies the area of several virtual detectors, thereby distorting the true diffuse signal. Blooming is a major problem that must be addressed for non-contact CCD-based diffuse optical imaging to be successful.

Figure 2: A pair of images illustrating what is known as CCD blooming. The approximate size of the laser beam is an ellipse of size 1mm x 1.5 (a). When the camera's integration time is increased the charge overflows from pixel wells in the position of the laser spot and into the neighboring wells (b). In this system blooming artifacts in the data make imaging large fluorescent targets difficult.

As mentioned previously, read-noise becomes a problem in low light scenarios, as is the case when the detectors are in far proximity from the active source. In general, it is well known that the signal intensity degrades by approximately 1OD for every 1cm from the location of the active source in diffuse optical imaging. So, data obtained at a detector say 3 cm from the source would inevitably be read-noise limited if they same integration time is used for all virtual detectors in the field-of-view. Subsequently, CCD-based DOT systems must take this into account. Here, this problem was accounted for by dividing the imaging ROI into three distinct bins according to integration time. With a base integration time of 50ms being used, a 10x increase in integration time was used for detectors located between 1-2cm of the source and a 100x integration time was used for detectors located within the 2-4cm region. This is schematically illustrated in Figure 3, where the detector integration scheme for cases of source 1 (a), 8 (b), and 16 (c) being active are depicted. In this system, a t_{int} of 50ms was selected under the assumption that the target fluorophore concentration would not exceed 10 μg/mL. Assuming this constraint is obeyed, the diffuse intensity at each virtual detector will be within the linear operating range of the CCD and blooming artifacts will not likely occur. In this study, which examined fluorescent targets having a range of sizes from 4-14mm, it was discovered that blooming was prevalent and a stable signal could not be obtained for large fluorescent targets (> 8 mm). The data collection scheme employed here permits fast acquisition and an adequate signal-to-noise to be obtained, yet a superior alternative would involve physically blocking the position of the active source so that blooming artifacts can be altogether eliminated.

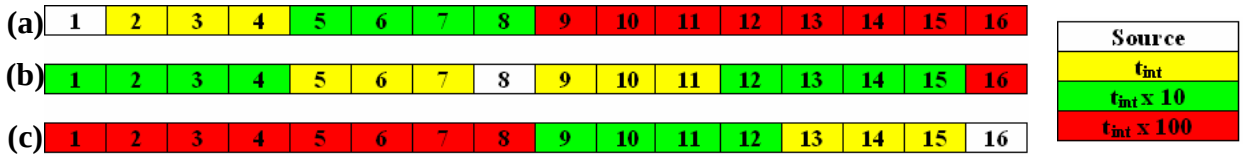

Figure 3: Examples of the optimal data acquisition scheme which involved reading the data out in three distinct bins. Here, the white rectangle represents the position of the active laser source, and the yellow, green, and red blocks represent integration time increases of 1x, 10x, and 100x respectively. This approach was necessary to maintain a suitable SNR at the detectors located far from the source. A t_{int} of 50ms was used in this work.

2.3 Theory of Image Formation

Images were reconstructed using NIRFAT [4, 10], an iterative, non-linear solver, which uses the finite-element method (FEM) to model light transport in tissue. Specifically, a nonlinear Newton-minimization approach to solving the frequency domain fluorescence diffusion approximation to the radiative transport equation (RTE) was utilized as the forward model [11]:

$$\nabla \cdot D_x(\vec{r})\nabla \Phi_x(\vec{r},\omega) - \left[\mu_{a\,x}(\vec{r}) + i\omega/c\right]\Phi_x(\vec{r},\omega) = -q_0(\vec{r},\omega) \tag{2}$$

$$\nabla \cdot D_m(\vec{r})\nabla \cdot \Phi_m(\vec{r},\omega) - \left[\mu_{a\,m}(\vec{r}) + i\omega/c\right]\Phi_m(\vec{r},\omega) = -\Phi_x(\vec{r},\omega)\eta\mu_{af}(\vec{r})\frac{1-i\omega\tau(\vec{r})}{1-[\omega\tau(\vec{r})]^2} \tag{3}$$

where Eq. (2) is the excitation field and Eq. (3) is the fluorescence emission field. The subscripts *x* and *m* denote the excitation and emission wavelengths respectively; $q_0(\vec{r},\omega)$ is an isotropic excitation source term at position $\vec{r}$; *c* is

the speed of light in the medium; ω is the modulation frequency at excitation; $\Phi_{x,m}(\vec{r},\omega)$ are the excitation and emission fields at position $\vec{r}$; $\mu_{a\,x}$ and μ_{am} represent the absorption coefficients; $\mu_{a\,f}$ is the absorption due to fluorophore; $D_{x,m} = 1/[3(\mu_{a\,x,m} + \mu'_{s\,x,m})]$ are the diffusion coefficients; τ is the fluorophore lifetime; and η is the fluorophore quantum efficiency. The reduced scattering coefficient, μ_s', is equivalent to $\mu_s(1-g)$, where g is the anisotropy factor μ_s is the scattering coefficient. Inverse solutions are then obtained by a modified spatially variant form of the Tikhonov approach as described previously [4, 12]. The mesh used to reconstruct all experimental images in this work contained 1600 elements and had dimensions of 60 mm (X-axis) by 30 mm (Y-axis). The X-dimension of the mesh was intentionally created to be slightly larger than the scan area in an effort to minimize boundary discrepancies between the experimental set-up and the medium – the forward data is essentially modeled as unbounded with respect to the location of the sources and detectors.

2.4 Simulation Studies

This simulation study was used to examine the ability for sub-surface tomography to recover target centroid position, size, and fluorophore concentration as a function of depth into the medium. NIRFAST was used to generate simulated fluorescence amplitude boundary data (1% noise added) and to produce subsurface fluorescence images. Target diameters in the range 4-14 mm having 10:1, 5:1, and 3.5:1 fluorescence contrasts were considered. The target centroid position was systematically adjusted over the range 0-15 mm for each. Mesh optical properties, $\mu_{a\,f}$ = 0.00205 mm^{-1}, $\mu_{a\,x}$ = 0.0071 mm^{-1}, μ_{sx} = 1 mm^{-1}, and an isotropic diffusion coefficient (D_x = 0.331 mm) were selected to mimic the background optical properties used in the liquid phantom experiments. Optical properties at the emission wavelength were set equal to those of the excitation wavelength. The refractive index for tissue was assumed to be n = 1.33 and the fluorophore lifetime (τ) was set to zero because amplitude only reconstructions were performed.

Target and background fluorophore concentrations used in the model were calculated by:

$$\mu_{af} = 2.303(\varepsilon \cdot c) \tag{5}$$

where μ_{af} is the absorbance, ε represents the molar extinction coefficient of Pp-IX, and c is the fluorophore concentration. In this work a Pp-IX molar extinction coefficient of 500 mm^{-1} M^{-1} [13]was used along with a Pp-IX molecular weight of 562.6 g/M in calculating the target and background fluorophore absorption values for use in these simulations. For the case of an 8mm target, the recovered target centroid position, size, and fluorophore concentration were quantified. The linearity in centroid position due to changes in target size, target-to-background contrast, and depth were also examined.

2.5 Phantom Studies

Fluorescence liquid phantom experiments were performed using a tissue simulating liquid phantom [4] and by submerging targets of different sizes over a range of depths at a fixed contrast. Data was acquired along a line at the bottom of the phantoms surface; images were then reconstructed in the plane perpendicular to that line. Using a mixture of water, intralipid (1%), ink (2%), Tween-20 (5%) and 1ug/ml Pp-IX, the optical properties of tissue in the presence of an exogenous contrast agent were simulated. In an effort to contrast the experimental and simulation studies without performing an exhaustive number of experiments, the absorption due to fluorophore in the target was fixed at 10:1 with respect to the background and data was acquired for targets of size 4mm, 8mm, and 14mm as the target centroid position was adjusted from 0mm to 10mm in 2.5mm increments. After the data was acquired it was calibrated and [4, 12] used to reconstruct the subsurface spatial distribution of fluorescence yield. The recovered centroid position was quantified and compared with simulation study results to assess the current technological limitations of subsurface diffuse optical tomography.

3. RESULTS

3.1 Simulation Studies

Simulation study results highlighting the recovered spatial distribution of fluorescence yield for an 8mm diameter target are depicted in Figure 4 for 3.5:1, 5:1, and 10:1 contrasts, for the ratio of target relative to the background. The target centroid position was adjusted between 0 and 10mm in 2.5 mm increments for each; the true locations of the target are shown at the bottom of this figure for comparison. This figure demonstrates that the target fluorophore concentration and size cannot be recovered in this geometry, as indicated by the large variation in these parameters with depth, but it does imply that the centroid location of the target can be recovered. In Figure 5, the recovered: $\eta\mu_{af}$ concentration (a), size (b), and centroid location (c) for the three contrasts under consideration are quantified as a function of depth into the medium. This figure confirms the empirical observation that target size and fluorophore concentration can not be recovered, but that the position of the target can be for realistic in-vivo contrasts. Specifically, for this case study of an 8 mm target, the mean error in centroid recovery was found to be 0.42 mm over the range 0-10 mm when all contrasts were considered. When the target depth was extended to 15mm, the mean positional accuracy in the recovered target was found to be 1.67 mm. These results have been demonstrated rigorously demonstrated in detail for fluorescence and absorbance subsurface imaging by Kepshire et al. [4].

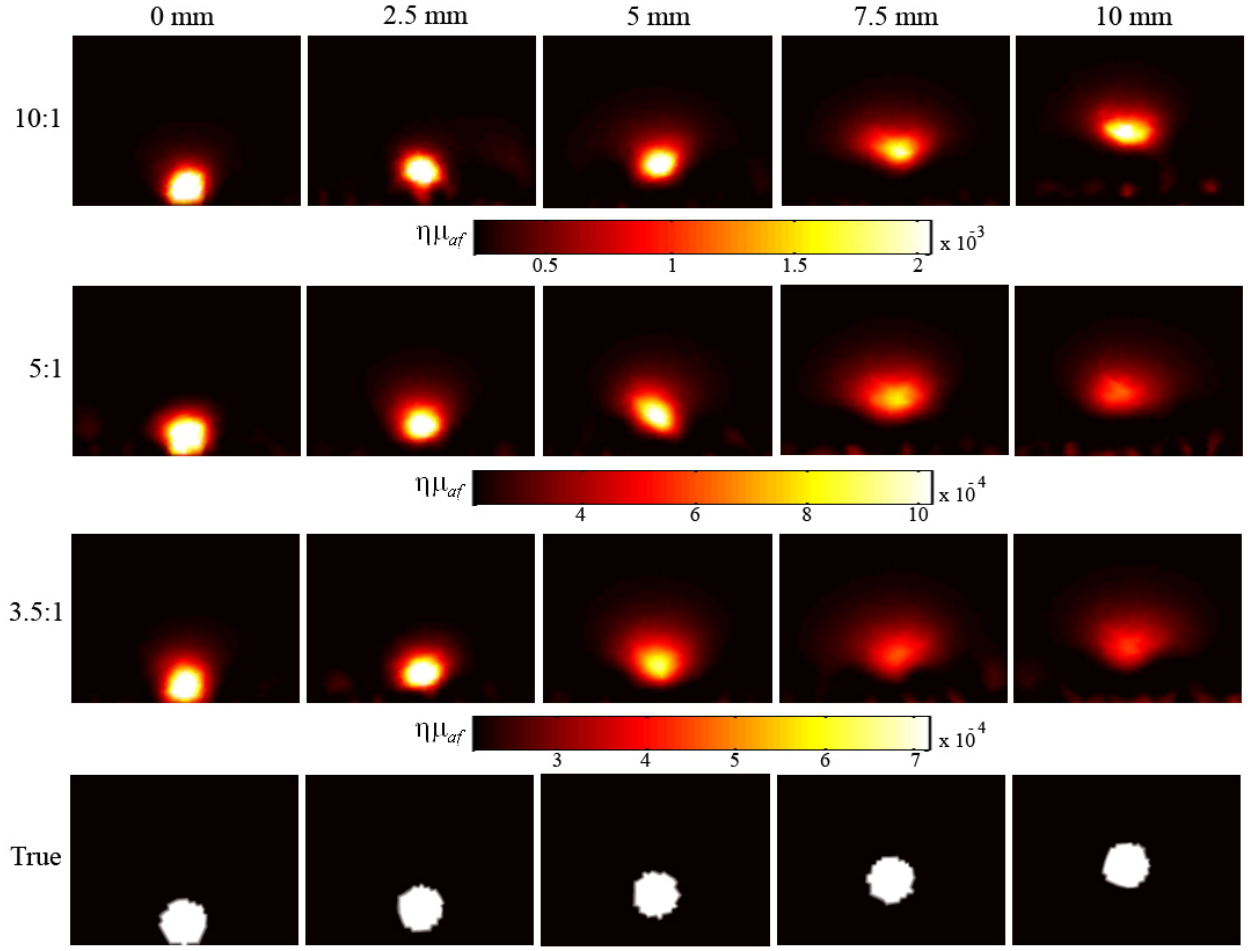

Figure 4: Simulation results for the recovered spatial distribution of fluorescence yield are depicted for an 8 mm anomaly having 10:1 ('effectively infinite'), 5:1, and 3.5:1 fluorescent contrast. In these images the location of the target is adjusted between 0 and 10mm, as indicated by the 'true images' shown at the bottom of this figure. This representative set of images illustrates that the ability to recover target size and $\eta\mu_{af}$ concentration degrades with increasing distance from the source/detector boundary. Again, it appears that the actual target location can be accurately estimated using the centroid technique.

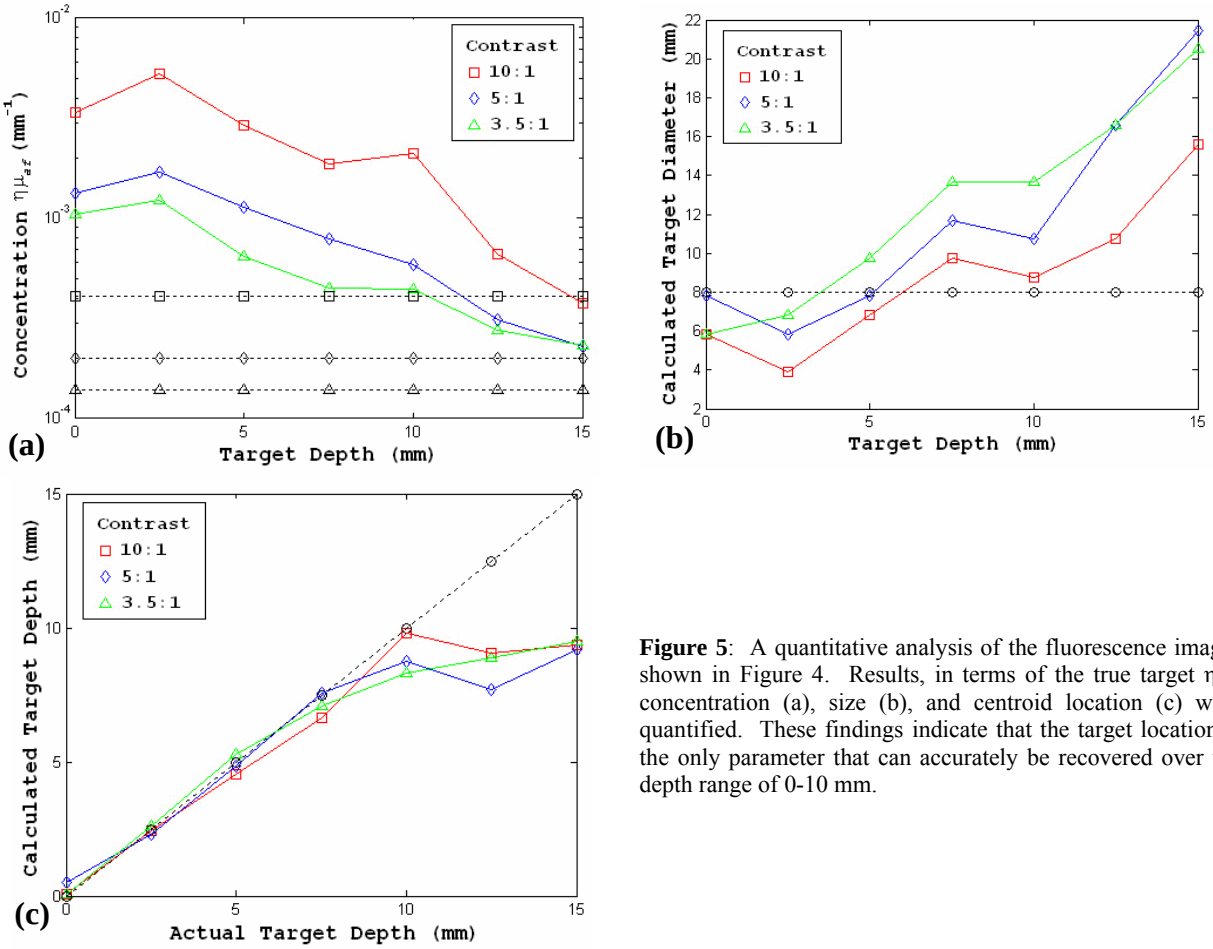

Figure 5: A quantitative analysis of the fluorescence images shown in Figure 4. Results, in terms of the true target $\eta\mu_{af}$ concentration (a), size (b), and centroid location (c) were quantified. These findings indicate that the target location is the only parameter that can accurately be recovered over the depth range of 0-10 mm.

To examine the impact of target size, fluorophore concentration, and depth on the ability to recover the centroid position of the target, a comprehensive study examining the error in recovered position was performed. Target sizes (4mm, 6mm, 8mm, 10mm, 12mm, & 14mm) and contrasts (3.5:1, 5:1, & 10:1) were considered as a function of depth in the range 0-10mm; the mean error in recovered position was determined for each. These results are summarized in Figure 5 for all contrasts and sizes at each of five depths (a), all sizes and depths for each contrast (b), and for all contrasts and depths for the six target sizes considered (c). In general, a linear increase in the calculated error can be observed with increasing target depth. Figure 6 (a) demonstrates this by depicting the total centroid error as a function of depth. In addition, from these plots it is clear that a non-linear response in centroid error can be observed when target contrast and size are considered. Specifically, in the case of error induced by variations in target contrast (Figure 5 (b)), a centroid error of less than 1.1 mm can be expected for biologically feasible fluorescent contrasts. The biphasic centroid error response induced by changes in target size can be observed in Figure 5 (c). From this one can infer that the recovered position for target diameters in the range 4-10 mm will be accurate to less than 1mm for all contrasts above 3.5:1 and centroid positions less than 1 cm. Increases in centroid error for larger targets (>1 cm) can likely be attributed to the size of the sampling region and the limited depths being probed. It is hypothesized that increasing the source/detector separation distance and thereby expanding the size of the sampling region, will likely improve the large target centroid error.

Figure 5: Plots depicting the centroid error response as a function of depth (a), contrast (b), and size (c). From these it is evident that error increases linearly with increases in target depth and non-linearly with changes in size contrast. Positional accuracy induced by changes in contrast are acceptable, but error increases rapidly for larger targets.

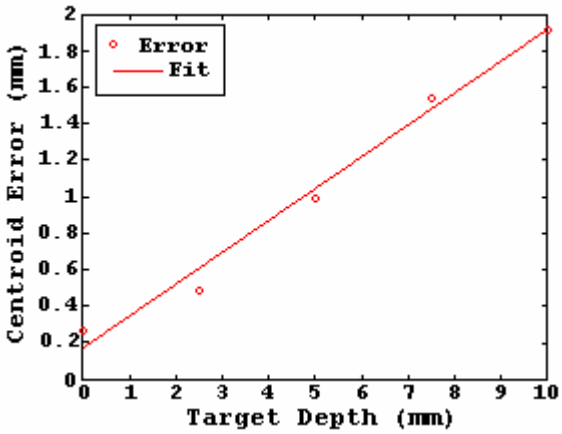

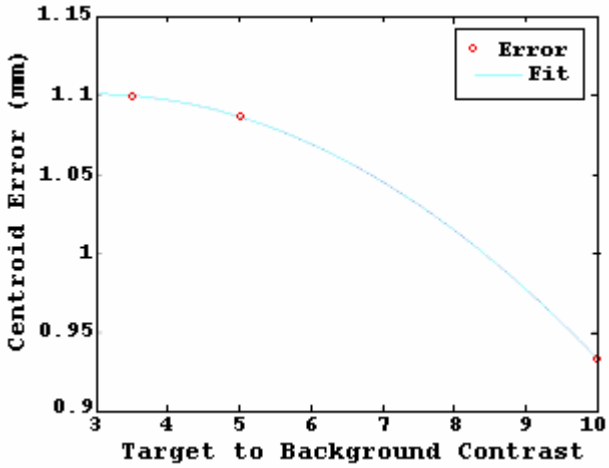

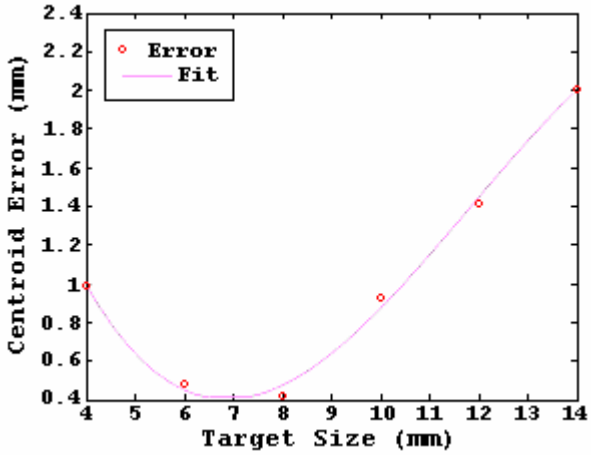

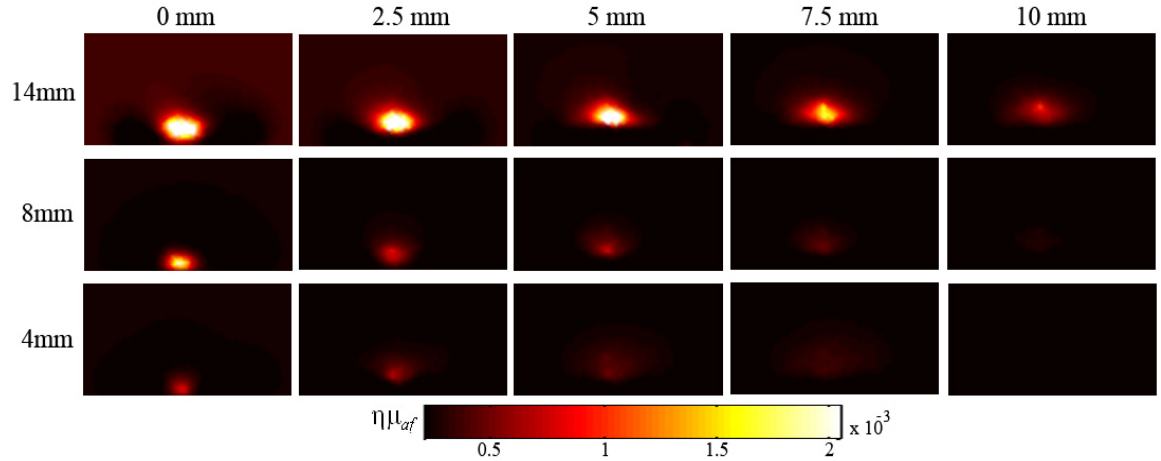

Figure 6: Images generated from experimental data for targets of size 14mm (top), 8mm (center), and 4mm (bottom). The contrast was fixed at 10:1 for each as the depth was adjusted from 0mm to 1cm.

3.2 Phantom Studies

The impact of target size on centroid accuracy was evaluated experimentally by fixing the fluorescence contrast at 10:1 while the size and position of the target were adjusted. Image reconstructions are depicted in Figure 6 for 14mm (top), 8mm (center), and 4mm (bottom) targets in the depth range of 0 – 10mm. Figure 7 (a) quantifies these results and compares them to simulation results (b) by graphically portraying the recovered centroid position for each size as a function of depth into the medium. Though the experimental results are substantially less accurate than the simulation results for the 4mm and 14mm targets, the same trends in the data are apparent – the recovered centroid location is underestimated for the 14mm target and overestimated for the 4mm target. Possible explanations for this will be presented in the following section – Discussion and Conclusions.

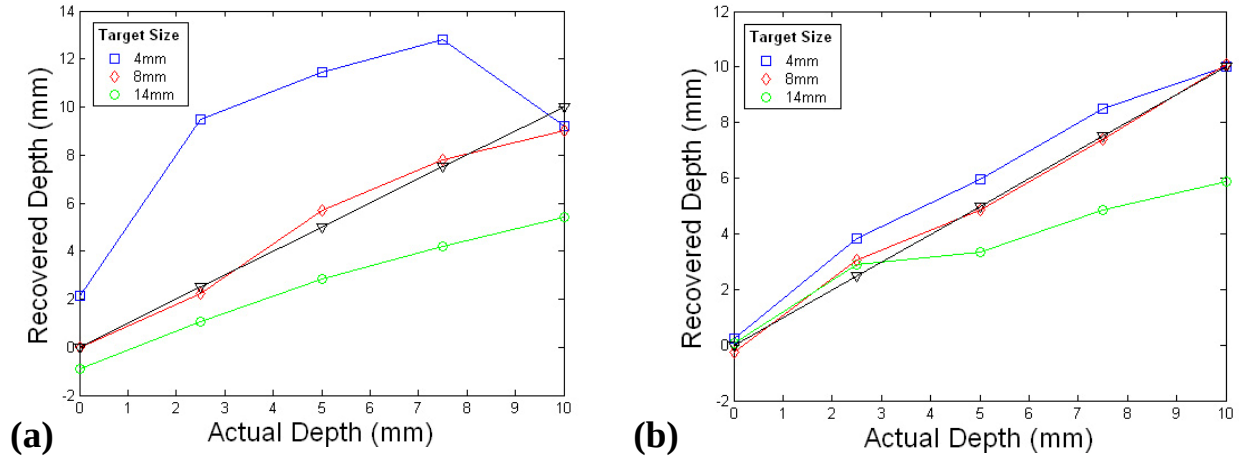

Figure 7: Experimental (a) and simulated (b) centroid results for a fixed target contrast of 10:1 for a range of sizes (4mm, 8mm, and 14mm) and depths (0-10mm).

4. DISCUSSION AND CONCLUSIONS

The signal attenuation constraint inherent to the remission mode geometry is the greatest limiting factor in this type of imaging, since the deeper projections through the tissue are simply too low to provide sufficient sensitivity at depths greater than 1 – 1.5 cm. As demonstrated by the simulation study results presented here, the centroid error is a function of target size, contrast, and depth into the medium.

There are two possible explanations for the large discrepancies between the simulated and experimental results presented here. One plausible explanation for this could be a poor SNR in the experimental data and two factors could be contributing to this – light piping around the outside of the acrylic cylindrical target and an inadequate CCD integration time. Regarding the light piping issue, because a clear acrylic cylinder with a 1mm wall thickness was used as the target, the propagation of the incident diffuse light would be inhibited from scattering through the acrylic walls into the region of increased fluorescent contrast. Specifically, the refractive index change between the intralipid mixture and the acrylic wall of the target gives rise to a reflection and a refraction of the incident light, with a significantly smaller percentage of the light being refracted. Subsequently, only a very small portion of the incident light reaches the inside of the target. By using a scattering material instead of an acrylic for the target, one can hypothesize that the experimental results could be improved significantly due to the improved SNR. In terms of SNR issues arising from a suboptimal integration time, the current integration scheme is optimized for imaging high contrast targets on the surface of the phantom. So, in imaging lower contrasts at depth, only a very small fraction of the camera's dynamic range is being utilized. Exploiting the full dynamic range of the camera is essential for maintaining a good SNR, but it is challenging because the fluorescence intensity rapidly degrades with decreasing target size, contrast, and depth. One possible solution for this would be to performing a series of 'fast-scans' where the same integration

time would be utilized for all detectors. In doing this, a poor signal-to-noise would exist at the read-noise limited detectors, but a good SNR would exist at the near-source detectors, which are the measurements of interest here. By then performing a linear fit to the maximum fluorescence intensity measurement in each fast-scan, the optimal integration time can easily be determined. To ensure linear operation of the CCD device, the integration time should be selected such that the maximum measurement consumes approximately 80-90% of the full well capacity. In dynamically adjusting the integration time an adequate SNR could easily be achieved in an in-vivo setting where no prior knowledge of the target size, contrast or depth is known.

In the case of the 14mm target's centroid being underestimated for both the simulation study and the experiments this is likely due to the fact that the spatially variant regularization implemented here was not optimized for recovering large targets. Also, because the top of the target is actually at a depth of 24mm when the target is located 1 cm from the surface, it is likely that the lack of sensitivity in this region inhibits accurate recovery by biasing the target to a more shallow depth. From an experimental perspective, the size of the imaging FOV and the source/detector separation distance used here may be hindering the target recovery because the entire depth of the target is not being probed.

For the 4mm target, experimental recovered centroid inaccuracies can likely be attributed to partial volume effects and light piping around the acrylic target. Partial volume effects are prevalent when small targets are being imaged because the acquired diffuse intensity signals at each detector constitute sampling from the background more so than from the target. Subsequently, the ability to detect and quantify subsurface lesions is inhibited. Increasing the number of detectors will reduce partial volume effects, but conversely it will result in increased computational requirements. Again, light piping around the acrylic target is most likely reducing the SNR or distorting the signal by preventing light from reaching the inside of the target.

The ability to provide an image reconstruction approach which is linear with depth in sub-surface mode may not be possible, without the addition object location from prior information obtained from another modality, such as ultrasound [14, 15], optical coherence tomography, x-ray, CT or MRI. The response of sub-surface diffuse reconstruction algorithms are depth dependent because of the ill-posed nature of diffuse imaging and the fact that the sensitivity decreases by orders of magnitude with increasing distance from the tissue surface[12]. Here, blooming artifacts are thought to have distorted the data in the case of a larger fluorescent targets. This could be corrected by projecting the diffuse signals onto a digital-micromirror (DMD) device before they are projected onto the CCD. The incorporation of a DMD would allow the CCD pixels corresponding to the position of actual source on the phantom to be turned off, so that blooming would not be an issue. Overall, the experimental results likely could be improved by using a more realistic tissue simulating phantom, as this would eliminate data artifacts introduced by light piping; partial volume related effects can only be improved or eliminated by increasing the detector density, or by incorporating prior structural information into the reconstruction.

5. ACKNOWLEDGEMENTS

This work has been funded by NCI grants RO1CA109558 and the Norris Cotton Cancer Center Shared Resources.

6. REFERENCES

1. Ntziachristos, V., et al., *Concurrent MRI and diffuse optical tomography of breast after indocyanine green enhancement.* Proceedings of the National Academy of Sciences of the United States of America, 2000. **97**(6): p. 2767-72.
2. Pogue, B.W., et al., *Quantitative Hemoglobin Tomography with Diffuse Near-Infrared Spectroscopy: Pilot Results in the Breast.* Radiology, 2001. **218**(1): p. 261-6.
3. Ntziachristos, V., et al., *MRI-guided diffuse optical spectroscopy of malignant and benign breast lesions.* Neoplasia, 2002. **4**(4): p. 347-54.
4. Kepshire, D.S., et al., *Sub-Surface Diffuse Optical Tomography can Localize Absorber and Fluorescent Objects but Recovered Image Sensitivity is Non-Linear with Depth.* Applied Optics, 2006. **(accepted)**.
5. Culver, J.P., et al., *Diffuse optical tomography of cerebral blood flow, oxygenation, and metabolism in rat during focal ischemia.* Journal of Cerebral Blood Flow & Metabolism, 2003. **23**(8): p. 911-24.

6. Franceschini, M. and D.A. Boas, *Noninvasive measurement of neuronal activity with near-infrared optical imaging.* NeuroImage, 2004. **21**: p. 372-386.
7. Hebden, J.C., et al., *Three-dimensional optical tomography of the premature infant brain.* Physics in Medicine & Biology, 2002. **47**(23): p. 4155-66.
8. Hebden, J.C., et al., *Imaging changes in blood volume and oxygenation in the newborn infant brain using three-dimensional optical tomography.* Physics in Medicine & Biology, 2004. **49**(7): p. 1117-30.
9. Chance, B., et al., *Breast Cancer Detection Based on Incremental Biochemical and physiological Properties of Breast Cancers: A Six-Year, Two-Site Study.* Academic Radiology, 2005. **12**(8): p. 925-933.
10. Davis, S.C., et al., *Contrast-detail analysis characterizing diffuse optical fluorescence tomography image reconstruction.* JBO Letters, 2005. **10**(5): p. 1-3.
11. Patterson, M.S. and B.W. Pogue, *Mathimatical model for time-resolved and frequency-domain fluorescence spectroscopy in biological tissues.* Appl. Opt., 1994. **33**(10): p. 1963-1974.
12. Kepshire, D., et al., *Sub-surface Fluorescence Imaging of Protoporphyrin IX with B-Scan Mode Tomography.* Proc. SPIE, 2006. **6139**: p. In Press.
13. Sharman, W.M., C.M. Allen, and J.E. van Lier, *Photodynamic therapeutics: basic principles and clinical applications.* Drug Discovery Today, 1999. **4**(11): p. 507-517.
14. Zhu, Q., N. Chen, and S.H. Kurtzman, *Imaging tumor angiogenesis by use of combined near-infrared diffusive light and ultrasound.* Optics Letters, 2003. **28**(5): p. 337-9.
15. Zhu, Q., et al., *Utilizing optical tomography with ultrasound localization to image heterogeneous hemoglobin distribution in large breast cancers.* Neoplasia, 2005. **7**(3): p. 263-70.